JACS
JOURNAL OF THE AMERICAN CHEMICAL SOCIETY

Article

pubs.acs.org/JACS

Metal–Organic Frameworks for Electrocatalytic Reduction of Carbon Dioxide

Nikolay Kornienko,[†,□] Yingbo Zhao,[†,□] Christopher S. Kley,[†] Chenhui Zhu,[⊥] Dohyung Kim,[‡] Song Lin,[†,#] Christopher J. Chang,[†,§,∥,#] Omar M. Yaghi,[*,†,∇,○,◆] and Peidong Yang[*,†,‡,∇,◆]

[†]Department of Chemistry, [‡]Department of Materials Science and Engineering, [§]Howard Hughes Medical Institute, and [∥]Department of Molecular and Cell Biology, University of California, Berkeley, California 94720, United States

[⊥]Advanced Light Source, [#]Chemical Sciences Division, and [∇]Materials Sciences Division, Lawrence Berkeley National Laboratory, Berkeley, California 94720, United States

[○]King Abdulaziz City of Science and Technology, P.O. Box 6086, Riyadh 11413, Saudi Arabia

[◆]Kavli Energy Nanosciences Institute, Berkeley, California 94720, United States

Supporting Information

ABSTRACT: A key challenge in the field of electrochemical carbon dioxide reduction is the design of catalytic materials featuring high product selectivity, stability, and a composition of earth-abundant elements. In this work, we introduce thin films of nanosized metal–organic frameworks (MOFs) as atomically defined and nanoscopic materials that function as catalysts for the efficient and selective reduction of carbon dioxide to carbon monoxide in aqueous electrolytes. Detailed examination of a cobalt–porphyrin MOF, $Al_2(OH)_2TCPP\text{-}Co$ (TCPP-H_2 = 4,4′,4″,4‴-(porphyrin-5,10,15,20-tetrayl)tetrabenzoate) revealed a selectivity for CO production in excess of 76% and stability over 7 h with a per-site turnover number (TON) of 1400. In situ spectroelectrochemical measurements provided insights into the cobalt oxidation state during the course of reaction and showed that the majority of catalytic centers in this MOF are redox-accessible where Co(II) is reduced to Co(I) during catalysis.

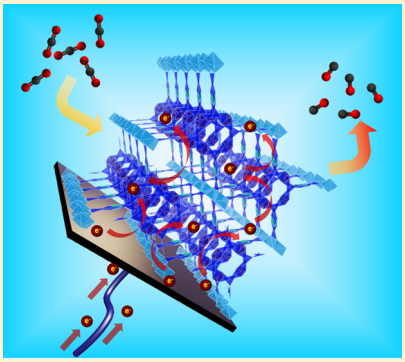

INTRODUCTION

One of the most attractive approaches toward providing carbon-neutral energy is the electrochemical conversion of atmospheric carbon dioxide (CO_2) into energy-dense carbon compounds to be used as fuels and chemical feedstock.[1−4] Extensive efforts have been devoted to the development of homogeneous and heterogeneous catalysts for this purpose. The outstanding challenges remain in the design of catalyst systems featuring (i) selectivity for CO_2 reduction in water with minimum H_2 generation, (ii) long-term stability, (iii) catalytic efficiency at low electrochemical overpotential, and (iv) compositions of earth abundant materials. In this report, we show that nanosized metal–organic frameworks (MOFs) meet these criteria and also present additional opportunities because of the modular nature of MOFs in which their organic and inorganic components can be functionalized and modified prior to precise arrangement in the MOF crystal structure.[5−12] We chose a stable cobalt porphyrin MOF where these porphyrin units are linked with aluminum oxide rods to form a 3D porous structure with pores of 6 × 11 Å^2. Electrochemical CO_2 reduction studies were carried out on thin films of this MOF, which was found to convert CO_2 to CO selectively (76% Faradaic efficiency) and with high turnover number (TON = 1400). In situ spectroelectrochemical measurements revealed that the Co(II) centers are reduced to Co(I) throughout the MOF and subsequently reduce CO_2. This is the first MOF catalyst constructed for the electrocatalytic conversion of aqueous CO_2 to CO, and its high-performance characteristics are encouraging for the further development of this approach.

In the context of aqueous electrocatalytic CO_2 reduction studies where heterogeneous catalysts such as metal foils,[13−17] metal nanostructures,[18−26] oxide-derived metals,[27−29] 2D materials,[30] carbon nanomaterials,[31−33] as well as bioinspired catalysts,[34−37] and homogeneous molecular catalysts[38−47] are used, MOFs combine the favorable characteristics of both heterogeneous and homogeneous catalysts. Exploration of MOFs for CO_2 reduction has just begun through their use as photocatalysts in colloidal dispersions, however, with the aid of sacrificial reagents,[48−52] and MOFs and COFs have only recently been utilized as electrocatalysts for CO_2 reduction.[53−56]

Our strategy to construct the MOF-based electrochemical CO_2 reduction system was to select MOFs with catalytic linker units and fabricate them into thin films covering conductive substrates (Figure 1): Appropriate catalytic linker units (Figure 1A) are assembled into a porous thin film MOF (Figures 1B and S1), which is grown on a conductive substrate (Figure 1C). We first screened MOFs with systematically varied building blocks and then chose the most promising MOF catalyst for in-

Received: August 4, 2015
Published: October 28, 2015

DOI: 10.1021/jacs.5b08212
J. Am. Chem. Soc. 2015, 137, 14129−14135

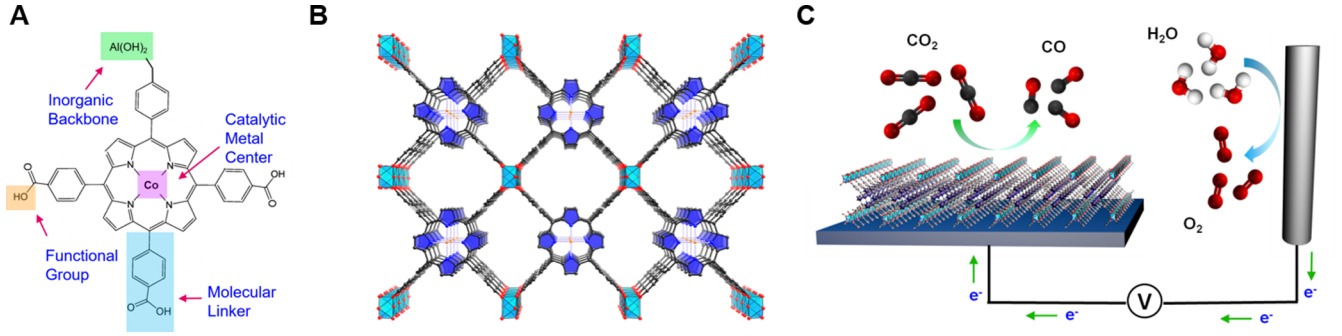

Figure 1. Our MOF catalyst allows for modulation of metal centers, molecular linkers, and functional groups at the molecular level (A). The organic building units, in the form of cobalt-metalated TCPP, are assembled into a 3D MOF, $Al_2(OH)_2TCPP\text{-}Co$ with variable inorganic building blocks (B). Co, orange spheres; O, red spheres; C, black spheres; N, blue spheres; Al, light-blue octahedra; and pyrrole ring, blue. In this structure, each carboxylate from A is bound to the aluminum inorganic backbone.The MOF is integrated with a conductive substrate to achieve a functional CO_2 electrochemical reduction system (C).

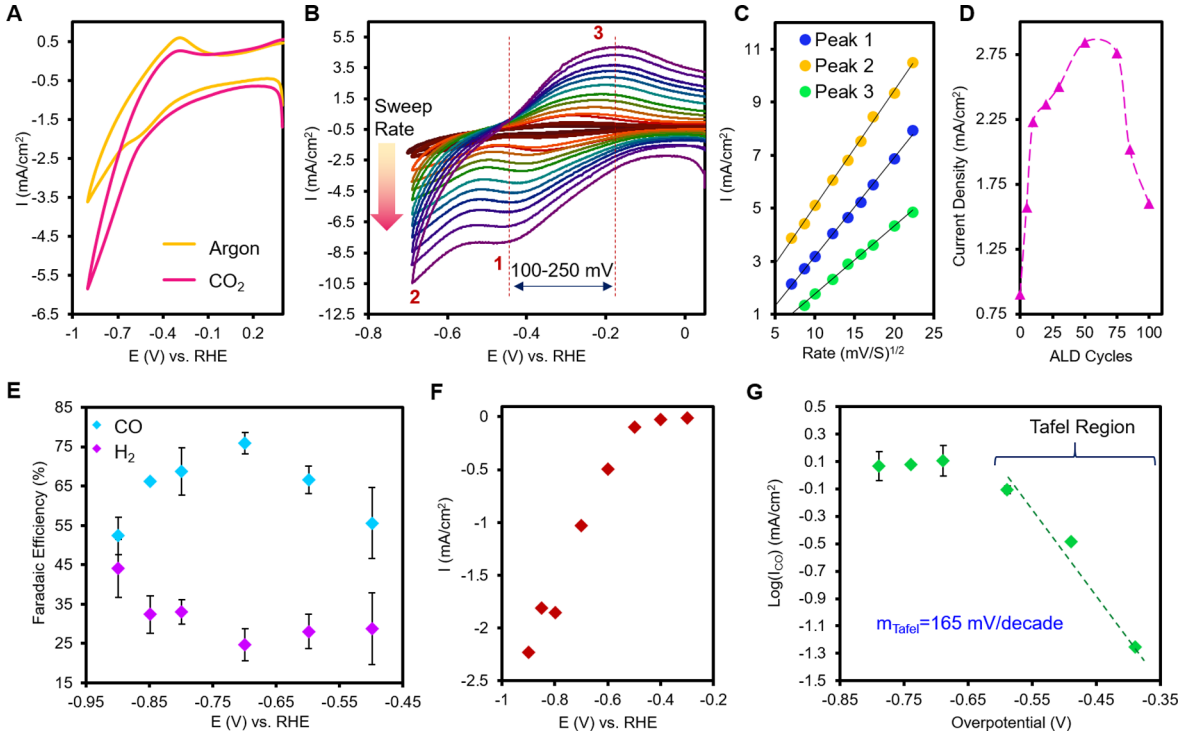

Figure 2. Voltammogram trace of the MOF catalyst exhibits a current increase in a CO_2 environment relative to an argon-saturated environment (A). As the scan rate is systematically increased in a CO_2-saturated electrolyte (B), the electrochemical waves increase in magnitude proportional to the square root of the scan rate (C), indicative of a diffusion-limited process. The MOF catalytic performance is maximized at a starting layer thickness of 50 ALD cycles (D), which offers a balance of charge transport, mass transport, and active-site density. The selectivity for each product is tested over a potential range of −0.5 to −0.9 vs RHE (E) and reaches upward of 76% for CO. The steady-state current density for product quantification is illustrated in F. In the low-overpotential region, the Tafel slope of 165 mV/decade is closest to that of a one-electron reduction from CO_2 to the CO_2· rate-limiting step (G).

depth electrochemical studies. The thickness of the selected MOF was next optimized to yield the final CO_2-reduction system, which was shown to be active, selective, and stable toward CO production. We also demonstrate that the majority of cobalt centers are reduced from Co(II) to Co(I) during the electrochemical process through in situ spectroelectrochemical measurements. Using MOFs as heterogeneous electrocatalysts represents an efficient strategy to reticulate catalytic molecular units into a porous network in which the number of active sites is maximized and both charge and mass transported could be simultaneously balanced by controlling the nanoscopic MOF morphology and thickness.

RESULTS AND DISCUSSION

The catalysts we selected in this work are the $Al_2(OH)_2TCPP\text{-}H_2$ series [TCPP-H_2 = 4,4′,4″,4‴-(porphyrin-5,10,15,20-tetrayl)tetrabenzoate], which incorporates the porphyrin-based molecular units previously reported as selective and efficient homogeneous CO_2-reduction electrocatalysts.[39,57,58] Specifically, the cobalt-metalated porphyrin units are known to be of particular interest for CO_2 reduction and are explored in detail in this work.[59−61] The advantage over using molecular porphyrins as homogeneous catalysts is that each active site is simultaneously exposed to the electrolyte and electrically connected to the conductive support. We employ our

DOI: 10.1021/jacs.5b08212
J. Am. Chem. Soc. 2015, 137, 14129−14135

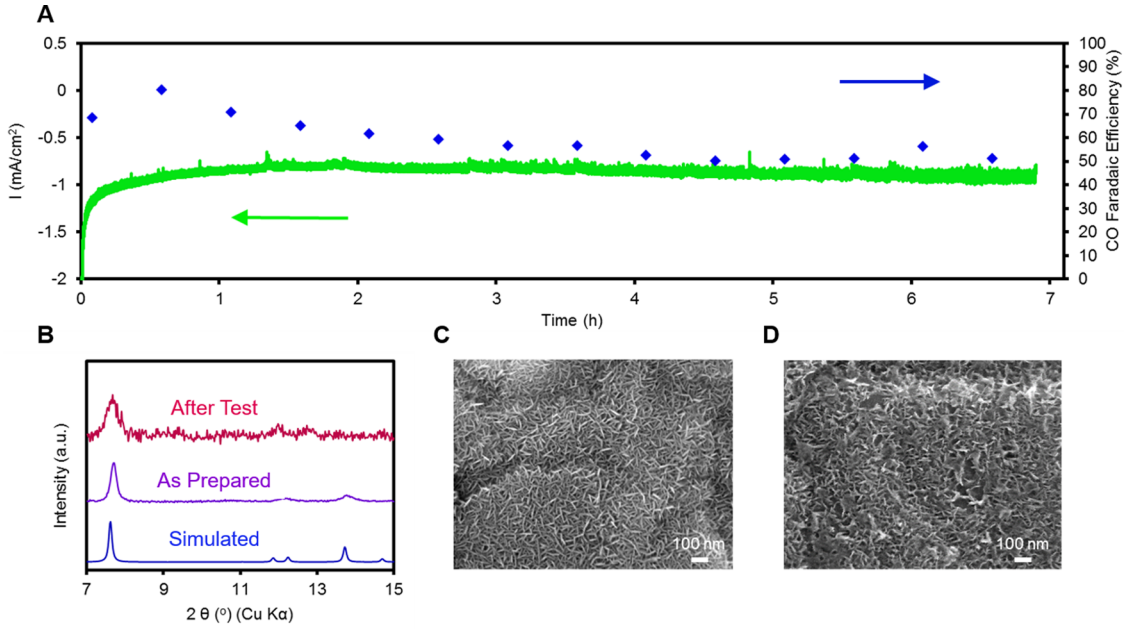

Figure 3. Stability of the MOF catalyst is evaluated through chronoamperometric measurements in combination with faradaic efficiency measurements. The green trace represents geometric current density, and the blue diamonds denote CO Faradaic efficiency (A). XRD analysis indicates that the MOF retains its crystalline structure after chronoamperometric measurement (B). SEM images of the MOF catalyst film before (C) and after electrolysis (D) reveal the retention of the platelike morphology.

previously developed methodology for thin-film MOF synthesis,[62] which involves the ALD deposition of metal oxide thin films as metal precursors onto the electrode and subsequent MOF creation through reacting the coated electrode with the appropriate linker in a DMF solvent in a microwave reactor.[63]

Initially, we studied the effect of employing different metal centers in the porphyrin units on the catalytic properties of the MOF (Figures S2 and S3). We began with 50 ALD cycles of alumina thin films (thickness of 5 nm) deposited onto conductive carbon disk electrodes, and converted the alumina film to porphyrin-containing MOF $[Al_2(OH)_2TCPP\text{-}M']$ structures with free-base porphyrin as well as porphyrin centers metalated with M′ = Zn, Cu, and Co. Cyclic voltammetry (CV) measurements of the synthesized metalated-porphyrin-containing MOFs under an argon or carbon dioxide environment were used to screen the MOF catalytic performance (Figure S2). The voltammogram traces feature redox waves attributed to the reduction of the metal centers and catalytic peaks stemming from the reduction of either protons or aqueous CO_2, qualitatively matching the behavior of previously studied analogous porphyrin homogeneous catalysts.[57] Notably, the cobalt-metalated MOF exhibits the highest relative increase in current density after saturating the solution with carbon dioxide (1 atm, 33 mM concentration), increasing from 3.5 to 5.9 mA/cm^2. Hence, this particular catalyst is chosen for further in-depth examination. Previous works have reported differences in activity and selectivity among porphyrins and porphyrin analogues with different metal centers, and cobalt was consistently among the best.[64,65] The increase in current density under a CO_2 atmosphere for this catalyst may be due to the preferred binding to CO_2 and increased kinetics of CO_2 reduction relative to hydrogen generation for this active site. To exhibit a further layer of modularity with our MOF-based catalyst design, we modified the inorganic backbone to prepare cobalt-metalated $[M_2(OH)_2TCPP\text{-}Co$, M = Al and In$]$ MOFs (Figures S4 and S5). The In- and In−Al-based MOF catalysts also exhibit significant current density increases under a CO_2-saturated aqueous bicarbonate electrolyte relative to an argon-bubbled electrolyte, suggesting that the porphyrin units are the essential catalytic active center and that the inorganic backbone may be tuned for additional purposes.

On the basis of our initial catalyst screening, we focused our subsequent investigation on the $[Al_2(OH)_2TCPP\text{-}Co]$ MOF. The voltammogram trace of this MOF showed an enhanced current density under a CO_2-saturated solution relative to that in an argon-saturated solution and displayed a redox couple in addition to an irreversible catalytic peak (Figure 2A). Increasing the CV scan rates (Figure 2B) illustrated that a cathodic wave centered roughly at −0.4 to −0.5 V versus the reversible hydrogen electrode (RHE), an irreversible catalytic peak immediately following, and an anodic peak at −0.2 V vs RHE increase in magnitude in a manner linearly proportional to the square root of the sweep rate, indicative of a diffusion-limited process (Figure 2C).[66,67] The first cathodic wave and the lone anodic wave are likely limited by counterion diffusion to balance a Co(II/I) redox change, and the irreversible cathodic peak, which is not voltammetric, at the most negative potentials stems from the diffusion and subsequent reduction of carbon dioxide. The anodic−cathodic wave separation increased from ∼100 to ∼250 mV with increasing sweep rate, which provided further evidence that the underlying reaction is not a simple reversible redox process. Previous electrochemical studies of cobalt porphyrins have attributed a cathodic wave at approximately −0.5 V vs RHE to the reduction of the Co(II) center to Co(I), and we see similar behavior for the homogeneous $H_4TCPP\text{-}Co$ (Figure S6).[68] Spectroelectrochemical studies confirmed the chemical nature of this cathodic wave as discussed below.

Balancing reactant diffusion and charge transport is essential for electrochemical catalysis. To this end, the thickness of the MOF catalyst film was tuned to optimize the performance of the MOF catalyst by varying the starting ALD alumina layer

DOI: 10.1021/jacs.5b08212
J. Am. Chem. Soc. 2015, 137, 14129−14135

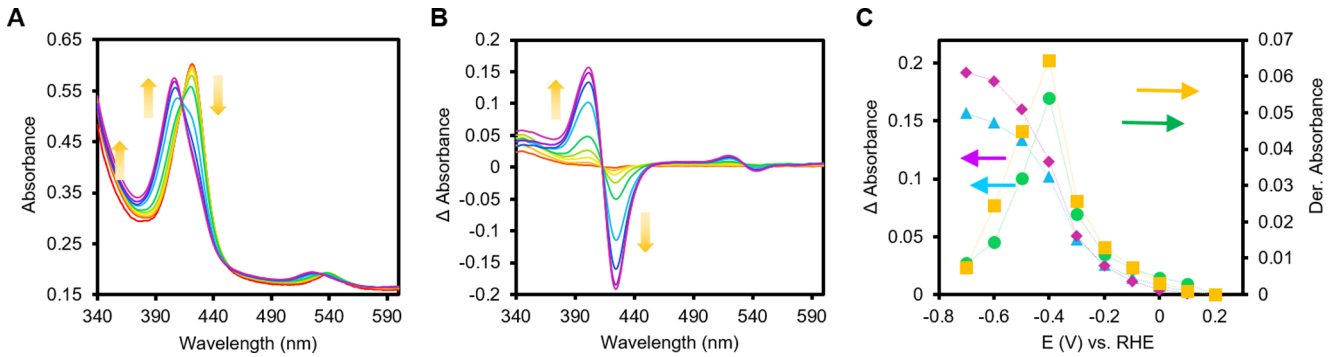

Figure 4. In situ spectroelectrochemical analysis reveals the oxidation state of the cobalt catalytic unit of the MOF under reaction conditions. Upon varying the voltage from 0.2 to −0.7 V vs RHE, the Co(II) Soret band decreases at 422 nm and is accompanied by a Co(I) Soret band increase at 408 nm (A). This change is quantified and plotted (B) to elucidate a formal redox potential of the Co center, which is deemed to be at the peak of the first derivative (C) of the Co(II) bleach and Co(I) enhancement.

thickness from 0.5 to 10 nm (Figure 2D). Upon testing a carbon disk electrode with only 5 layers (0.5 nm) of ALD precursor converted to the MOF, resulting in an ∼10 nm thick MOF layer, we observed a twofold increase in the catalytic current density (measured at −0.57 V vs RHE at a sweep rate of 100 mV/s) relative to that of the bare carbon disk substrate. The performance of the MOF catalyst increased with increasing active-site loading until reaching a maximum at 50 ALD cycles (MOF thickness of ∼30−70 nm). Inductively coupled plasma atomic emission absorption (ICP-AES) was utilized to quantify the total cobalt loading on this sample and indicated an upper limit of 6.1×10^{16} cobalt atoms (1.1×10^{-7} mol) per square centimeter. The performance decrease observed for higher active-site loading is likely due to charge-transport limitations from the electrode to the MOF periphery or impedance through a thin insulating alumina layer not fully converted to the MOF. This result highlights the strength of our ALD-based MOF conversion technique, which allows nanometer precision of catalyst loading to balance active-site density with mass/charge transfer.

Comprehensive product analysis using gas chromatography (GC) and nuclear magnetic resonance (NMR) was carried out to reveal the nature of the chemical processes occurring within our MOF catalysts (Figure S7). As illustrated in Figure 2E, the two main products measured were CO and H_2, with current selectivity for CO reaching up to 76% at −0.7 V vs RHE. The average steady-state current density from these measurements is displayed in Figure 2F. In contrast, the unmetalated MOF produces primarily H_2 (Figure S8). When plotting the partial current density for CO production on a logarithmic scale versus the thermodynamic overpotential (Figure 2G), we obtain a Tafel slope of 165 mV/decade in the low-overpotential region, which points to a one-electron reduction of CO_2 to form the $CO_2^{\cdot}$ radical as a probable rate-limiting step, though the reaction is likely to be at least in part diffusion-limited.[16,69−71] However, the exact nature of the rate-limiting step is difficult to determine from the Tafel slope alone, especially in a more complicated system such as ours. For comparison, studies of porphyrin homogeneous catalysts have measured Tafel slopes ranging from 100 to 300 mV/decade; thus, the rate-limiting step and mechanism may depend on more than just the active site itself.[72−74] We stress that this is the first incarnation of our MOF electrocatalyst, and efforts are being undertaken to further exploit the modular nature of such systems for the next generation of catalyst.

The stability of the MOF catalyst was next tested over an extended period of time. In controlled potential electrolysis at −0.7 V vs RHE in CO_2-saturated aqueous bicarbonate buffer, the current density reached a stable state after several minutes and subsequently showed no sign of decrease for up to 7 h, generating 16 mL of CO (0.71 mmol, 5.25 cm^2 substrate; Figures 3A, S8, and S9). The lower limit of the TON of the MOF catalyst is quantified through ICP analysis of the electrode after testing and is determined to be 1400 assuming every cobalt atom is an electrochemically active site (turnover frequency (TOF) ≈ 200 h^{-1}). The MOF largely retains its crystallinity after electrolysis, and preservation of the framework was evidenced through the retention of the major powder X-ray diffraction (XRD) peaks (Figure 3B). Furthermore, scanning electron microscopy (SEM) analysis reveals that the platelike morphology has been retained (Figure 3C,D). In situ surface-enhanced Raman spectroscopy (SERS) was utilized to confirm the integrity of the organic units throughout the catalytic process (Figure S11). At each applied potential, the primary SERS peaks attributed to the porphyrin linker remain in the SERS spectrum.

In situ spectroelectrochemical testing was next employed to ascertain the cobalt oxidation state under operating conditions. Such techniques have proven valuable for studying the electronic structure of porphyrins.[68,75−81] We grew the MOF on a transparent conductive fluorine-doped tin oxide (FTO) substrate and measured the film's UV−vis absorbance for a series of applied electrochemical potentials (Figure 4A). A typical absorption of the cobalt-metalated $[Al_2(OH)_2TCPP\text{-}Co]$ MOF in open-circuit states featured a Soret band ($S_0 \rightarrow S_2$) at 422 nm and a Q band ($S_0 \rightarrow S_1$) at 530 nm. The increase in absorbance at lower wavelengths has also been attributed to the back-donation of Co(I) into the porphyrin system.[60] Upon applying increasingly negative potential (0 to −0.7 V vs RHE) to the FTO/MOF electrode in a CO_2-saturated electrolyte, the Soret band under steady-state conditions decreases in intensity at 422 nm and increases at 408 nm, with isosbestic points at 413 and 455 nm (Figure 4A). Plotting the difference spectra (Figure 4B) illustrates the band bleach and increase in the aforementioned spectral regions, which is subsequently quantified to deduce the formal redox potential ($E_{1/2}$) of the cobalt center in our system. The peak in the first derivative of the difference magnitude in these two wavelengths signified the formal reduction potential of the cobalt porphyrin unit in the MOF at −0.4 V vs RHE (Figure 4C), which is consistent with the position of the first cathodic wave in the voltammogram

DOI: 10.1021/jacs.5b08212
J. Am. Chem. Soc. 2015, 137, 14129−14135

trace. However, even at potentials more positive than −0.4 V vs RHE, a fraction of the cobalt centers are still reduced and are likely to be participating in the catalytic conversion of CO_2 to CO.

The buildup of a Co(I) species under operating conditions and a Tafel slope of 165 mV/decade indicates that the rate-limiting step in our reaction mechanism may be either a CO_2 molecule adsorbing onto a Co(I) porphyrin coupled with a one-electron reduction or a one-electron reduction of a Co(I)−CO_2 adduct. We stress the importance of this spectroelectrochemical data in signifying that the majority of the cobalt centers are electrically connected to the electrode and are reduced to the catalytically active Co(I) state.

■ CONCLUDING REMARKS

We have demonstrated the applicability of MOF-integrated catalytic systems as modular platforms for the electrochemical reduction of aqueous CO_2. This study represents the development of our first generation of MOF-based CO_2 reduction electrocatalysts in which the active site, inorganic backbone, and thickness/loading were rationally chosen and the resulting MOF integrated onto a conductive support. The modularity of these systems yields many opportunities to further improve performance and open new directions in electrocatalysis.

■ EXPERIMENTAL SECTION

Chemicals. N,N-Dimethylformamide (DMF) (99.8%), dimethyl sulfoxide (DMSO) (99.5%), anhydrous acetonitrile, potassium carbonate, and cobalt(II) acetate tetrahydrate were purchased from Sigma-Aldrich. FTO substrates (7 Ω/sq) were purchased from Sigma-Aldrich and cut on site into desirable dimensions. Aluminum chloride hexahydrate (99.9%) was purchased from Fluka. Ethanol was purchased from KOPTEC. 4,4′,4″,4‴-(Porphyrin-5,10,15,20-tetrayl)-tetrabenzoic acid (H_4TCPP) was purchased from TCI. 2-Methylimidazole (99%) and biphenyl-4,4-dicarboxylic acid (97%) were purchased from Aldrich. Trimethylaluminum and trimethylindium were purchased from Strem chemicals. Hydrochloric acid and anhydrous DMF were purchased from EMD Millipore. Sodium hydroxide and methanol were purchased from Fischer chemical. Carbon disk substrates were purchased from Ted Pella. All chemicals were used as received without further purification.

Atomic Layer Deposition. Atomic layer deposition (ALD) was carried out with a home-built thermal ALD system. Trimethylaluminum, trimethylindium, and water were used as aluminum, indium, and oxygen sources, respectively. Precursors were held in customized vessels to allow for pulsed delivery. Alumina deposition was carried out at 150 °C, and indium oxide deposition was carried out at 200 °C. Pulse times for trimethylaluminum, trimethylindium, and water were 1.0, 2.0, and 0.5 s, respectively. Nitrogen functioned as both a purge and carrier gas and was flowed at a rate of 10 cm^3/min. Following the desired amount of ALD cycles, the chamber was purged with nitrogen, and the samples were taken out and allowed to cool naturally to room temperature in an air environment. The calibration of the amorphous alumina growth rate was previously carried out with TEM measurements on a variety of surfaces and was consistently 0.1 nm/cycle.

Powder X-ray Diffraction. Powder X-ray diffraction (PXRD) patterns were acquired with a Bruker D8 Advance diffractometer (Cu Kα radiation, λ = 1.54056 Å).

UV−Vis Spectroscopy. The optical absorption spectra were recorded using a UV−vis−NIR scanning spectrophotometer equipped with an integration sphere (Shimadzu UV-3101PC). A quartz cuvette functioned as a one-compartment electrochemical cell with a Ag/AgCl reference and Pt-wire counter electrode.

MOF Synthesis. Following the ALD coating on the desired substrate, no further modifications were made, and the substrate as-made was put through the MOF synthesis. MOF synthesis was carried out in pyrex microwave vials using a CEM Discover-SP W/Activent microwave reactor. In a typical synthesis, the desired ALD-coated sample was mixed with 5 mg of H_4TCPP, 1.5 mL of DMF, and 0.5 mL of water. The vessel was heated to 140 °C for 10 min. Following this, the sample was allowed to naturally cool to room temperature and washed with DMF and ethanol. Further purification was carried out by soaking the sample for 4 days in DMF and exchanging the liquid daily. After the DMF soak, the samples were soaked in acetone for 1 day and held under vacuum at room temperature for one more day. The growth of the MOF thin films is believed to occur via a dissolution−recrystallization mechanism. XRD, UV−vis absorption, HRTEM, and grazing incidence wide-angle X-ray scattering (GIWAXS) measurements all confirmed the identity and phase purity of the MOF.

Electrochemistry. For all experiments, 0.5 M potassium carbonate was used as the electrolyte. Prior to electrochemical testing, the electrolyte was purified overnight by applying 2 V potential difference between working and counter Ti foil electrodes to remove trace metal salts and organic species. A standard 3-electrode setup was employed with a titanium counter electrode and Ag/AgCl reference electrode. For product quantification, a home-built two-compartment setup was used that featured a nafion membrane separating the working and counter compartments. All current densities are normalized by projected surface areas.

Gas Chromatography. A home-built electrochemical cell was utilized for quantitative product measurement. The cell had two compartments separated by a nafion membrane to prevent product oxidation at the counter electrode. A flow mode was used to quantify gas products. Liquid products were quantified after the electrochemical measurement. During the chronoamerometric measurement, gas from the cell was directed through the sampling loop of a gas chromatograph (SRI) and was analyzed in 20 min intervals. The gas chromatograph was equipped with a molecular sieve (13X) and hayesep D column with Ar (Praxair, 5.0 ultrahigh purity) flowing as a carrier gas. The separated gas products were analyzed by a thermal conductivity detector (for H_2) and a flame ionization detector (for CO and gaseous hydrocarbons). Liquid products were analyzed afterward by quantitative NMR (Bruker AV-500) using dimethyl sulfoxide as an internal standard.

ICP-AES. ICP-AES was carried out on a PerkinElmer optical emission spectrometer Optima 7000DV instrument. A carbon disk (5.25 cm^2) coated with the MOF was put in the bottom of a 20 mL glass vial with an acid-resistant cap. A 2 mL aliquot of 99.5% nitric acid was then added to the vial and reacted violently with the carbon disk, where the carbon disk was exfoliated and deformed. A substantial amount of heat was released during the process, and orange smoke, presumably NO_2, was generated. Two minutes later, 2 mL of deionized water was added to dilute the acid so that the oxidation of the carbon disk was terminated. This solution was kept for 3 days to completely digest the MOF. Next, 4 mL of deionized water was added to the vial to further dilute the nitric acid. The clear solution for ICP measurement was obtained by centrifuging this carbon−nitric acid mixture at 4400 rpm for 1 min and collecting the supernatant. The concentration of cobalt in this solution was determined to be 3.8 ppm with approximately 10% error, giving a total cobalt amount of 30.4 μg, which was calculated to be 5.1×10^{-7} M. Considering the overall surface area of 5.25 cm^2 on the carbon disk, the cobalt loading on carbon disk was 6.1×10^{16} cobalt atoms per square centimeter.

Spectroelectrochemistry. FTO-coated glass (7 Ω/sq) was utilized as a transparent conducting substrate for in situ spectroelectrochemical measurements. The alumina deposition and conversion to MOF procedure was identical to that used for the carbon disk substrate. A quartz 5 mL cell served as a one-compartment electrochemical cell, with Ag/AgCl and Pt serving as reference and counter electrodes, respectively. The cell was filled with 0.5 M carbonate buffer saturated with carbon dioxide prior to measurements, and a carbon dioxide atmosphere was maintained throughout. The FTO working electrode was held at the desired potential for 3 min to reach steady-state conditions before acquiring a spectrum. A

DOI: 10.1021/jacs.5b08212
J. Am. Chem. Soc. 2015, 137, 14129−14135

Shimadzu-3101 PC spectrometer fitted with an integrating sphere was used for all measurements.

Raman Spectroscopy. Raman measurements are carried out on a Horiba Labram JY HR 800 with an Olympus SMPLN 100× objective. A 532 nm diode laser was utilized as an excitation source. An open one-compartment cell served as the in situ cell for the measurement with Ag/AgCl and Pt functioning as the reference and counter electrodes, respectively. The electrolyte used was 0.5 M potassium bicarbonate, saturated with carbon dioxide. SERS substrates were fabricated through electrochemically roughening silver films. First, 300 nm of silver was thermally evaporated onto a titanium foil substrate. Next, the silver was electrochemically roughened through oxidation−reduction cycles in 3 M potassium chloride electrolyte. The silver-coated titanium electrode was cycled 10 times between −1.2 and 0.3 V vs RHE at 50 mV/second. All SERS measurements were conducted under steady-state conditions.

Grazing Incidence Wide Angle X-ray Scattering. GIWAXS spectra were acquired with a Pilatus 2 M (Dectris) instrument on beamline 7.3.3 at the Advanced Light Source, Lawrence Berkeley National Laboratory (λ = 1.24 Å). The incidence angle was held at 0.120 to optimize signal collection. Silver behenate was used to calibrate the sample−detector distance and the beam center. The Nika package for IGOR Pro (Wavemetrics) was utilized to reduce the acquired 1D raw data to a 2D format.

Because of the fact that the carbon disks are covered by the salt precipitating from the electrolyte after electrolysis, the GIWAXS measurements on those samples are not successful because of the strong scattering of the residue salts near the surface on high angle saturating the detector. The SEM images are also influenced by the presence of the salt.

■ ASSOCIATED CONTENT

Supporting Information

The Supporting Information is available free of charge on the ACS Publications website at DOI: 10.1021/jacs.5b08212.

Experimental details, additional structural, electrochemical, and spectroscopic characterization. (PDF)

■ AUTHOR INFORMATION

Corresponding Authors

*yaghi@berkeley.edu

*p_yang@berkeley.edu

Author Contributions

□N.K. and Y.Z. contributed equally.

Notes

The authors declare no competing financial interest.

■ ACKNOWLEDGMENTS

Electron microscopy was carried out at the National Center of Electron Microscopy (NCEM), which is supported by the Office of Science, Office of Basic Energy Sciences of the U.S. Department of Energy (DOE) under contract no. DE-AC02-05CH11231. Work at the Molecular Foundry was supported by the Office of Science, Office of Basic Energy Sciences, of the U.S. Department of Energy under Contract No. DE-AC02-05CH11231. This research was partially supported by BASF SE (Ludwigshafen, Germany) for synthesis of MOF, and King Abdulaziz City of Science and Technology (Riyadh, Saudi Arabia) for electrochemical characterization. Financial support for nanocrystal catalysis in P.Y.'s laboratory work was supported by the Director, Office of Science, Office of Basic Energy Sciences, Materials Science and Engineering Division, U.S. Department of Energy under contract no. DE-AC02-05CH11231(Surface). O.M.Y. is thankful to Dr. Turki Al Saud (KACST) for his continued input and interest. Grazing incidence wide-angle X-ray scattering (GIWAXS) measurements were carried out at the Advanced Light Source (ALS) at Lawrence Berkeley National Lab (LBNL). The ALS is an Office of Science User Facility operated for the U.S. DOE, Office of Science, by LBNL and supported by the U.S. DOE under contract no. DE-AC02-05CH11231. Y.Z. is supported by the Suzhou Industrial Park fellowship. C.S.K. acknowledges support by the Alexander von Humboldt Foundation. Financial support for energy catalysis in the C.J.C. laboratory (S.L. and C.J.C.) was provided by U.S. Department of Energy (DOE)/Lawrence Berkeley National Laboratory (LBNL) grant 101528-002. C.J.C. is an Investigator with the Howard Hughes Medical Institute.

■ REFERENCES

(1) Appel, A. M.; Bercaw, J. E.; Bocarsly, A. B.; Dobbek, H.; DuBois, D. L.; Dupuis, M.; Ferry, J. G.; Fujita, E.; Hille, R.; Kenis, P. J.; et al. *Chem. Rev.* **2013**, *113*, 6621.

(2) Aresta, M.; Dibenedetto, A.; Angelini, A. *Chem. Rev.* **2014**, *114*, 1709.

(3) Costentin, C.; Robert, M.; Savéant, J.-M. *Chem. Soc. Rev.* **2013**, *42*, 2423.

(4) Quadrelli, E. A.; Centi, G.; Duplan, J. L.; Perathoner, S. *ChemSusChem* **2011**, *4*, 1194.

(5) Yaghi, O. M.; Li, H.; Davis, C.; Richardson, D.; Groy, T. L. *Acc. Chem. Res.* **1998**, *31*, 474.

(6) Yaghi, O. M.; O'Keeffe, M.; Ockwig, N. W.; Chae, H. K.; Eddaoudi, M.; Kim, J. *Nature* **2003**, *423*, 705.

(7) Lee, J.; Farha, O. K.; Roberts, J.; Scheidt, K. A.; Nguyen, S. T.; Hupp, J. T. *Chem. Soc. Rev.* **2009**, *38*, 1450.

(8) Zhou, H.-C.; Long, J. R.; Yaghi, O. M. *Chem. Rev.* **2012**, *112*, 673.

(9) Kuppler, R. J.; Timmons, D. J.; Fang, Q.-R.; Li, J.-R.; Makal, T. A.; Young, M. D.; Yuan, D.; Zhao, D.; Zhuang, W.; Zhou, H.-C. *Coord. Chem. Rev.* **2009**, *253*, 3042.

(10) Wang, Z.; Cohen, S. M. *Chem. Soc. Rev.* **2009**, *38*, 1315.

(11) An, J.; Rosi, N. L. *J. Am. Chem. Soc.* **2010**, *132*, 5578.

(12) Kitagawa, S.; Kitaura, R.; Noro, S. i. *Angew. Chem., Int. Ed.* **2004**, *43*, 2334.

(13) Hori, Y.; Murata, A.; Takahashi, R. *J. Chem. Soc., Faraday Trans. 1* **1989**, *85*, 2309.

(14) DeWulf, D. W.; Jin, T.; Bard, A. J. *J. Electrochem. Soc.* **1989**, *136*, 1686.

(15) Rosen, B. A.; Salehi-Khojin, A.; Thorson, M. R.; Zhu, W.; Whipple, D. T.; Kenis, P. J.; Masel, R. I. *Science* **2011**, *334*, 643.

(16) Kuhl, K. P.; Cave, E. R.; Abram, D. N.; Jaramillo, T. F. *Energy Environ. Sci.* **2012**, *5*, 7050.

(17) Hoshi, N.; Kato, M.; Hori, Y. *J. Electroanal. Chem.* **1997**, *440*, 283.

(18) Kim, D.; Resasco, J.; Yu, Y.; Asiri, A. M.; Yang, P. *Nat. Commun.* **2014**, *5*, 4948.

(19) Zhu, W.; Michalsky, R.; Metin, O. n.; Lv, H.; Guo, S.; Wright, C. J.; Sun, X.; Peterson, A. A.; Sun, S. *J. Am. Chem. Soc.* **2013**, *135*, 16833.

(20) Zhu, W.; Zhang, Y.-J.; Zhang, H.; Lv, H.; Li, Q.; Michalsky, R.; Peterson, A. A.; Sun, S. *J. Am. Chem. Soc.* **2014**, *136*, 16132.

(21) Zhang, S.; Kang, P.; Meyer, T. J. *J. Am. Chem. Soc.* **2014**, *136*, 1734.

(22) Manthiram, K.; Beberwyck, B. J.; Alivisatos, A. P. *J. Am. Chem. Soc.* **2014**, *136*, 13319.

(23) Gao, D.; Zhou, H.; Wang, J.; Miao, S.; Yang, F.; Wang, G.; Wang, J.; Bao, X. *J. Am. Chem. Soc.* **2015**, *137*, 4288.

(24) Medina-Ramos, J.; Pupillo, R. C.; Keane, T. P.; DiMeglio, J. L.; Rosenthal, J. *J. Am. Chem. Soc.* **2015**, *137*, 5021.

(25) Medina-Ramos, J.; DiMeglio, J. L.; Rosenthal, J. *J. Am. Chem. Soc.* **2014**, *136*, 8361.

(26) Lu, Q.; Rosen, J.; Zhou, Y.; Hutchings, G. S.; Kimmel, Y. C.; Chen, J. G.; Jiao, F. *Nat. Commun.* **2014**, *5*, 3242.

(27) Li, C. W.; Kanan, M. W. *J. Am. Chem. Soc.* **2012**, *134*, 7231.

DOI: 10.1021/jacs.5b08212
J. Am. Chem. Soc. 2015, 137, 14129−14135

(28) Chen, Y.; Kanan, M. W. *J. Am. Chem. Soc.* **2012**, *134*, 1986.
(29) Chen, Y.; Li, C. W.; Kanan, M. W. *J. Am. Chem. Soc.* **2012**, *134*, 19969.
(30) Asadi, M.; Kumar, B.; Behranginia, A.; Rosen, B. A.; Baskin, A.; Repnin, N.; Pisasale, D.; Phillips, P.; Zhu, W.; Haasch, R.; et al. *Nat. Commun.* **2014**, *5*, 4470.
(31) Wu, J.; Yadav, R. M.; Liu, M.; Sharma, P. P.; Tiwary, C. S.; Ma, L.; Zou, X.; Zhou, X.-D.; Yakobson, B. I.; Lou, J.; et al. *ACS Nano* **2015**, *9*, 5364.
(32) Zhang, S.; Kang, P.; Ubnoske, S.; Brennaman, M. K.; Song, N.; House, R. L.; Glass, J. T.; Meyer, T. J. *J. Am. Chem. Soc.* **2014**, *136*, 7845.
(33) Kumar, B.; Asadi, M.; Pisasale, D.; Sinha-Ray, S.; Rosen, B. A.; Haasch, R.; Abiade, J.; Yarin, A. L.; Salehi-Khojin, A. *Nat. Commun.* **2013**, *4*, 2819.
(34) Liu, C.; Gallagher, J. J.; Sakimoto, K. K.; Nichols, E. M.; Chang, C. J.; Chang, M. C.; Yang, P. *Nano Lett.* **2015**, *15*, 3634.
(35) Torella, J. P.; Gagliardi, C. J.; Chen, J. S.; Bediako, D. K.; Colón, B.; Way, J. C.; Silver, P. A.; Nocera, D. G. *Proc. Natl. Acad. Sci. U. S. A.* **2015**, *112*, 2337.
(36) Reda, T.; Plugge, C. M.; Abram, N. J.; Hirst, J. *Proc. Natl. Acad. Sci. U. S. A.* **2008**, *105*, 10654.
(37) Schuchmann, K.; Müller, V. *Science* **2013**, *342*, 1382.
(38) Seshadri, G.; Lin, C.; Bocarsly, A. B. *J. Electroanal. Chem.* **1994**, *372*, 145.
(39) Costentin, C.; Drouet, S.; Robert, M.; Savéant, J.-M. *Science* **2012**, *338*, 90.
(40) Smieja, J. M.; Sampson, M. D.; Grice, K. A.; Benson, E. E.; Froehlich, J. D.; Kubiak, C. P. *Inorg. Chem.* **2013**, *52*, 2484.
(41) Fujita, E.; Haff, J.; Sanzenbacher, R.; Elias, H. *Inorg. Chem.* **1994**, *33*, 4627.
(42) Thoi, V. S.; Kornienko, N.; Margarit, C. G.; Yang, P.; Chang, C. J. *J. Am. Chem. Soc.* **2013**, *135*, 14413.
(43) Kang, P.; Cheng, C.; Chen, Z.; Schauer, C. K.; Meyer, T. J.; Brookhart, M. *J. Am. Chem. Soc.* **2012**, *134*, 5500.
(44) Schneider, J.; Jia, H.; Kobiro, K.; Cabelli, D. E.; Muckerman, J. T.; Fujita, E. *Energy Environ. Sci.* **2012**, *5*, 9502.
(45) Tornow, C. E.; Thorson, M. R.; Ma, S.; Gewirth, A. A.; Kenis, P. J. *J. Am. Chem. Soc.* **2012**, *134*, 19520.
(46) Richardson, R. D.; Holland, E. J.; Carpenter, B. K. *Nat. Chem.* **2011**, *3*, 301.
(47) Lacy, D. C.; McCrory, C. C.; Peters, J. C. *Inorg. Chem.* **2014**, *53*, 4980.
(48) Wang, C.; Xie, Z.; deKrafft, K. E.; Lin, W. *J. Am. Chem. Soc.* **2011**, *133*, 13445.
(49) Fu, Y.; Sun, D.; Chen, Y.; Huang, R.; Ding, Z.; Fu, X.; Li, Z. *Angew. Chem.* **2012**, *124*, 3420.
(50) Liu, Y.; Yang, Y.; Sun, Q.; Wang, Z.; Huang, B.; Dai, Y.; Qin, X.; Zhang, X. *ACS Appl. Mater. Interfaces* **2013**, *5*, 7654.
(51) Li, L.; Zhang, S.; Xu, L.; Wang, J.; Shi, L.-X.; Chen, Z.-N.; Hong, M.; Luo, J. *Chem. Sci.* **2014**, *5*, 3808.
(52) Wang, D.; Huang, R.; Liu, W.; Sun, D.; Li, Z. *ACS Catal.* **2014**, *4*, 4254.
(53) Hinogami, R.; Yotsuhashi, S.; Deguchi, M.; Zenitani, Y.; Hashiba, H.; Yamada, Y. *ECS Electrochem. Lett.* **2012**, *1*, H17.
(54) Kumar, R. S.; Kumar, S. S.; Kulandainathan, M. A. *Electrohem. Commun.* **2012**, *25*, 70.
(55) Hod, I.; Sampson, M. D.; Deria, P.; Kubiak, C. P.; Farha, O. K.; Hupp, J. T. *ACS Catal.* **2015**, 6302.
(56) Lin, S.; Diercks, C. S.; Zhang, Y.-B.; Kornienko, N.; Nichols, E. M.; Zhao, Y.; Paris, A. R.; Kim, D.; Yang, P.; Yaghi, O. M.; Chang, C. J. *Science* **2015**, *349*, 1208.
(57) García, M.; Aguirre, M. J.; Canzi, G.; Kubiak, C. P.; Ohlbaum, M.; Isaacs, M. *Electrochim. Acta* **2014**, *115*, 146.
(58) Bonin, J.; Chaussemier, M.; Robert, M.; Routier, M. *ChemCatChem* **2014**, *6*, 3200.
(59) Leung, K.; Nielsen, I. M.; Sai, N.; Medforth, C.; Shelnutt, J. A. *J. Phys. Chem. A* **2010**, *114*, 10174.
(60) Behar, D.; Dhanasekaran, T.; Neta, P.; Hosten, C.; Ejeh, D.; Hambright, P.; Fujita, E. *J. Phys. Chem. A* **1998**, *102*, 2870.
(61) RamÍRez, G.; Lucero, M.; Riquelme, A.; Villagrán, M.; Costamagna, J.; Trollund, E.; Aguirre, M. J. *J. Coord. Chem.* **2004**, *57*, 249.
(62) Zhao, Y.; Kornienko, N.; Liu, Z.; Zhu, C.; Asahina, S.; Kuo, T.-R.; Bao, W.; Xie, C.; Hexemer, A.; Terasaki, O.; Yang, P.; Yaghi, O. M. *J. Am. Chem. Soc.* **2015**, *137*, 2199.
(63) Reboul, J.; Furukawa, S.; Horike, N.; Tsotsalas, M.; Hirai, K.; Uehara, H.; Kondo, M.; Louvain, N.; Sakata, O.; Kitagawa, S. *Nat. Mater.* **2012**, *11*, 717.
(64) Tripkovic, V.; Vanin, M.; Karamad, M.; Björketun, M. r. E.; Jacobsen, K. W.; Thygesen, K. S.; Rossmeisl, J. *J. Phys. Chem. C* **2013**, *117*, 9187.
(65) Qiao, J.; Liu, Y.; Hong, F.; Zhang, J. *Chem. Soc. Rev.* **2014**, *43*, 631.
(66) Bard, A. J.; Faulkner, L. R. *Electrochemical Methods: Fundamentals and Applications*; Wiley: New York, 1980.
(67) Newman, J.; Thomas-Alyea, K. E. *Electrochemical Systems*; John Wiley & Sons: Hoboken, NJ, 2012.
(68) Ahrenholtz, S. R.; Epley, C. C.; Morris, A. J. *J. Am. Chem. Soc.* **2014**, *136*, 2464.
(69) Russell, P.; Kovac, N.; Srinivasan, S.; Steinberg, M. *J. Electrochem. Soc.* **1977**, *124*, 1329.
(70) Bandi, A. *J. Electrochem. Soc.* **1990**, *137*, 2157.
(71) Hatsukade, T.; Kuhl, K. P.; Cave, E. R.; Abram, D. N.; Jaramillo, T. F. *Phys. Chem. Chem. Phys.* **2014**, *16*, 13814.
(72) Riquelme, M.; Isaacs, M.; Lucero, M.; Trollund, E.; Aguirre, M.; Canales, J. *J. Chil. Chem. Soc.* **2003**, *48*, 89.
(73) Najafi, M.; Sadeghi, M. *ECS Electrochem. Lett.* **2013**, *2*, H5.
(74) Manbeck, G. F.; Fujita, E. *J. Porphyrins Phthalocyanines* **2015**, *19*, 45.
(75) Kung, C.-W.; Chang, T.-H.; Chou, L.-Y.; Hupp, J. T.; Farha, O. K.; Ho, K.-C. *Chem. Commun.* **2015**, *51*, 2414.
(76) Kadish, K.; Boisselier-Cocolios, B.; Coutsolelos, A.; Mitaine, P.; Guilard, R. *Inorg. Chem.* **1985**, *24*, 4521.
(77) Wei, Z.; Ryan, M. D. *Inorg. Chim. Acta* **2001**, *314*, 49.
(78) Lin, X.; Boisselier-Cocolios, B.; Kadish, K. *Inorg. Chem.* **1986**, *25*, 3242.
(79) Quezada, D.; Honores, J.; García, M.; Armijo, F.; Isaacs, M. *New J. Chem.* **2014**, *38*, 3606.
(80) Kadish, K. M.; Van Caemelbecke, E. *J. Solid State Electrochem.* **2003**, *7*, 254.
(81) Kadish, K. M.; Smith, K. M.; Guilard, R., Eds. *The Porphyrin Handbook*; Academic Press: San Diego, CA, 1999.

DOI: 10.1021/jacs.5b08212
J. Am. Chem. Soc. 2015, 137, 14129−14135